MEMS-VCSEL as a tunable light source for OCT imaging of long working distance

Mohammed S. Khan,[a] **Changdae Keum**,[a,b] **Yi Xiao**,[a,c] **Keiji Isamoto**,[a] **Nobuhiko Nishiyama**,[b] **and Hiroshi Toshiyoshi**[c,*]

[a]Santec Corporation, Optical Imaging and Sensing Company, Tokyo, Japan
[b]Tokyo Institute of Technology, Department of Electrical and Electronic Engineering, Tokyo, Japan
[c]The University of Tokyo, Institute of Industrial Science, Tokyo, Japan

Abstract. We present a wavelength tunable vertical-cavity surface-emitting laser (VCSEL) constructed by die-bonding a half-cavity InGaAs laser diode (LD) chip onto a silicon-on-insulator chip with a microelectromechanical system electrostatic diaphragm mirror that functions as a Fabry–Perot interferometer. As a result of the short cavity length, the integrated tunable LD has single-mode lasing characteristics with an extremely large coherence length of 150 m or more. The developed wavelength tunable LD is used to perform swept-source optical coherence tomography with a large scan depth, which is applicable to ophthalmic observation for the diagnosis of pathologic nearsightedness based on the measurement of the axial length of an eye. [DOI: 10.1117/1.JOM.1.3.034503]

Keywords: wavelength tunable laser diode; microelectromechanical system; vertical-cavity surface-emitting laser; optical coherence tomography.

Paper 21011 received Jun. 10, 2021; accepted for publication Aug. 17, 2021; published online Aug. 31, 2021.

1 Introduction

Myopia or nearsightedness is an ophthalmologic disorder that causes blurred vision and is usually corrected by wearing glasses or contact lenses.[1] When staring at nearby objects for extended periods of time, the ophthalmic lenses are deformed through tension in the musculus ciliaris and may temporarily have trouble focusing on a distant object. This type of nearsightedness is called refractive myopia or pseudomyopia, and it can be cured naturally over time or by medication that relaxes the tension in the musculus ciliaris, thereby allowing the lens to revert to the normal thickness. Due to the outbreak of COVID-19, the statistics in 2020 reported an increasing number of refractive myopia cases that have been possibly caused by environmental factors, including extended time spent performing desk-work and limited exposure to outdoor light.[2]

Pathologic nearsightedness or axial myopia, on the other hand, is more aggressive in nature and caused by the abnormal extension of the ocular fundus. The stage of progression of this ocular disorder is diagnosed by measuring the axial length between the cornea surface and the retina as schematically defined in Fig. 1. Due to the elongation of the axial length, which normally falls in a range between 22 and 25 mm,[1] the focal point of the eye is anomalously shifted off of the retina, reducing the clarity of visual perception. Axial myopia can also be associated with more serious intercurrent pathologies, including scleral staphyloma, glaucoma, and myopic macular degeneration, sometimes leading to schisis and retinal tears.[1] These syndromes possibly result in blindness, and it is therefore crucial to diagnostically distinguish cases of axial myopia from refractive myopia at the earliest possible age. At present, no definitive therapy or medication has been found to cure axial myopia, except for a few positive reports with low-concentration dosing of atropine (0.01%) is effective for schoolchildren to suppress further elongation of the axial length.[3,4] For this reason, ophthalmologic assessment of the axial length is being

*Address all correspondence to Hiroshi Toshiyoshi, hiro@iis.u-tokyo.ac.jp

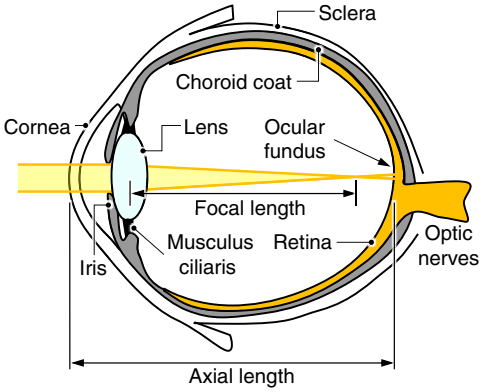

Fig. 1 Schematic illustration of ocular structure exhibiting axial myopia. Abnormal elongation of the axial length causes pathological shortsightedness.

included in a large-scale vision-check on 9000 schoolchildren, organized by the Japan Ministry of Education, Culture, Sports, Science, and Technology (MEXT) for the next three years starting in 2021.

Time-of-flight measurement of ultrasonic waves is usually used to determine the axial length of the eye, calculating the distances to the tissue boundaries that reflect the ultrasonic waves.[5] For measurement, an ultrasonic probe sensor is brought into direct contact with the cornea surface or indirectly coupled with it using an eyecup filled with water. In either case, extreme caution must be used when handling the equipment to avoid injuring the delicate tissue, as well as to prevent ocular infections.

From a hygienic point of view, optical measurement of the axial length is preferable when performing pre-symptomatic checkups on large populations. Currently, the refractive power of the eye can be measured using, for instance, an auto refractometer/keratometer,[6] and advanced versions of such instruments are equipped with a function to monitor the radius of curvature of the ocular fundus for further inspection. Fundoscopy based on optical coherence tomography (OCT) is a more powerful method to visualize the detailed tissue cross-section.[7,8] OCT is an imaging technology that acquires tomographic visual information similar to that provided by ultrasonic or x-ray computer tomography (x-ray CT) with imaging resolutions up to a few microns, which is finer than that of ultrasonic imaging by an order of magnitude. Compared with x-ray CT, OCT is more suitable for clinical and biological applications because it relies on infrared light and is therefore free from harmful radiation exposure.

In this paper, we review the fundamental principle of OCT and discuss a methodology to extend the measurement depth using a highly coherent light source. As an alternative method to the classic time-domain OCT (TD-OCT) measurement, in which the length of the reference arm in the optical interferometer is mechanically modulated, we use a wavelength tunable laser diode (LD) to perform Fourier-domain OCT or so-called swept-source OCT (SS-OCT). As a key component for such SS-OCT systems, we have developed a wavelength tunable LD using a microelectromechanical system (MEMS)-based electrostatic mirror that is coupled with a vertical-cavity surface-emitting laser (VCSEL) chip, which was originally invented by Iga and documented in detail in his recent review paper published elsewhere,[9] forming a Fabry–Perot interferometer. Owing to the single-mode resonance, the coherence length and coherence revival length are extended, thereby enabling OCT observation through an object as large as the entire ocular globe with single-shot imaging. This paper includes extended results such as the large coherence length over 150 m, based on the precedent technical report presented at IEEE OMN 2019.[10]

2 OCT Principle

The fundamental measurement method leading to OCT was developed in 1987 by Takada et al.,[7] who demonstrated detection of failure in an optical waveguide that was formed into an

interferometer illuminated by a low-coherence super luminescent diode (SLD); the methodology was called optical coherence-domain reflectometry, which was later used for ophthalmologic ocular diameter measurement at a high resolution of 10 μm. In 1991, Huang et al.[8] with MIT published a paper on OCT, which lead to the rapid development of OCT-related technologies, including ophthalmic measurement instruments on a commercial level in the 1990s. OCT today is widely accepted not only in the field of ophthalmology but also in cardiology,[11] dentistry,[12] and dermatology.[13] Non-contact OCT is also preferred for industrial applications, such as laser welding monitoring[14] and light-detection-and-ranging (LiDAR).[15]

Figure 2 illustrates a simplified analytical model for OCT measurement based on the Michelson–Morley interferometer. The probe light emitted from a light source is split into two branches: the reference arm and the sample arm. The light traveling in the reference arm is bounced back by the reflector and guided into the photodetector (PD) after traveling a round-trip distance of $2(z + \Delta z_r)$, where Δz_r is the adjustable position of the reflector. The electrical field of the light at the PD is written as[16,17]

$$E_r = A_r e^{i\{\omega t - 2k(z+\Delta z_r)\}}, \tag{1}$$

where A_r is the amplitude of the wave, t is the time lapse for the travel, and ω is the angular frequency of the light that is related to the speed of light c and the wave number k by $c = \omega/k$. In a similar manner to the reference path, the electrical field of the sampled light at the PD is written as

$$E_s = A_s e^{i\{\omega t - 2k(z+\Delta z_s)\}}, \tag{2}$$

where A_s is the amplitude of the wave and Δz_s is the optical length to the depth of the reflection center, taking the refractive index of the surrounding medium into account.

When these two lights interfere, the total optical power received by the PD is calculated by the product of complex conjugates as

$$P_d = (E_r + E_s)(E_r + E_s)^* = A_r^2 + A_s^2 + 2A_r A_s \cos 2k(\Delta z_s - \Delta z_r). \tag{3}$$

The first two terms are the dc components that can be eliminated using a balanced PD, and the third term depends on the difference between the two optical path lengths $2(\Delta z_s - \Delta z_r)$ as well as the wavenumber of the probe light $k = 2\pi/\lambda$, where λ is the wavelength.

OCTs in the early stage used low coherence light sources with relatively broad bandwidths, such as SLDs[7] and multi-mode lasers. Owing to the multiple modes contained within a bandwidth as schematically shown in Fig. 3(a), the waveform of light traveling in the space is described by the repetition of wave packets as shown in Fig. 3(b). Such a wave maintains its spatial coherence within the limited range along the traveling axis called the coherence length. Presuming a Gaussian distribution of laser power with a bandwidth of $\Delta\lambda_{BW}$, the coherence length is written as[16]

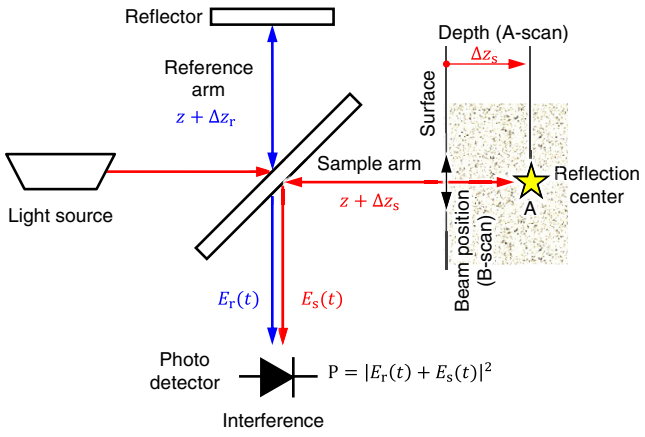

Fig. 2 Principle of OCT based on the Michelson–Morley interferometer.

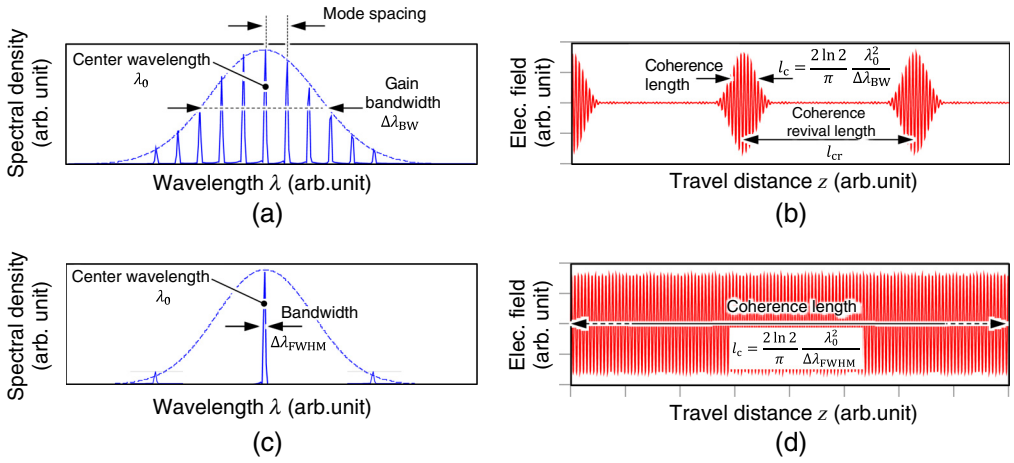

Fig. 3 Coherence length affected by the mode of the light source. (a) Spectral density of a multimode light source with Gaussian distribution and (b) its electrical field waveform along the axis of travel. Coherence is maintained only within the periodic coherence length. (c) Spectral density of a single-mode light source and (b) its electrical field waveform.

$$l_c = \frac{2\ln 2}{\pi}\frac{\lambda^2}{\Delta\lambda_{BW}}. \tag{4}$$

Therefore, the wider the bandwidth $\Delta\lambda_{BW}$ is, the shorter the coherence length l_c becomes. In a classic OCT system, the reference path length is adjusted to fulfill the matching condition $\Delta z_s = \Delta z_r$ so that the lights from the reference and the sample arms constructively interfere to intensify the signal level by

$$\cos 2k(\Delta z_s - \Delta z_r) = \cos 0 = 1. \tag{5}$$

This occurs within the short coherence length, thereby enabling the precise measurement of the reflection center's depth Δz_s.

In practical implementations of TD-OCT systems, the position of the reference reflector Δz_r is mechanically modulated to seek the peak OCT signal, and the resolution of the resulting spatial measurement is limited by the coherence length or the positioning precision of the reference reflector. Given a bandwidth $\Delta\lambda_{BW}$ is 50 nm around a center wavelength λ of 1050 nm, the coherence length l_c is expected to be 9.7 μm, which is comparable with the typical dimension of a biological cell. In OCT technology, the longitudinal scan to search for the depth of the reflection point is called the A-scan, whereas the lateral beam position control over the sample surface is called the B-scan as shown in Fig. 2. The orthogonal set of A- and B-scans, therefore, produces cross-sectional or volumetric images.

Due to the modulation mechanism of the reflector in the reference arm, the frame rate of TD-OCT is usually no faster than 30 fps.[18] Aside from the penetration depth of light in the sample, the scan depth is usually limited by the mechanical stroke of the reflector, typically a few millimeters or less. Another limiting factor for the depth of an OCT scan is more inherent to the nature of the coherence of light. Given a representative cavity length L in the laser unit, the round-trip distance within the cavity, $2L$, should be a multiple of the lasing wavelength λ to maintain the oscillation, and therefore the phase shift after a round trip is written as

$$\phi = 2\pi\frac{2L}{\lambda} = 2\pi\frac{2L\nu}{c} = 2\pi m, \tag{6}$$

where m is a positive integer, and ν is the oscillation frequency ($\nu = c/\lambda$). Under this condition, the difference of the phase shift $\Delta\phi$ between an adjacent pair of resonant modes is 2π, that is,

$$\Delta\phi = 2\pi\frac{2L\Delta\nu}{c} = 2\pi, \tag{7}$$

and hence the spacing between the modes is written in terms of frequency as

$$\Delta\nu = \frac{c}{2L}, \tag{8}$$

which is usually called the free-spectral range (FSR).

Superposition of multiple modes (ν, $\nu + \Delta\nu$, $\nu + 2\Delta\nu$, $\cdots$) produces a beat in the oscillation envelope at a base tone frequency of $\Delta\nu$; this envelope fluctuation manifests as the wave packets that repeatedly appear at a constant interval of $\Delta\nu^{-1}$ in the time domain or at a constant spatial pitch called the coherence revival length $l_{\mathrm{cr}} = c/\Delta\nu = 2L$ in the space domain as shown in Fig. 3(b). As a result, the OCT signal intensifies not only at the phase matching condition of $\Delta z_{\mathrm{s}} = \Delta z_{\mathrm{r}}$ but also at multiple positions that fulfill $\Delta z_{\mathrm{s}} = \Delta z_{\mathrm{r}} + mL$, which causes ghost-like artifact images at false depths. The effect of coherent revival is more pronounced when the tunable cavity length L is as large as a few millimeters to a centimeter, for instance, in the case of an external cavity laser.[19,20] Hence, TD-OCT optics with low coherence LDs have high axial resolution owing to the short coherence length but imaging depth is limited to a few millimeters.

When a VCSEL structure is adopted for a light source, on the other hand, the tunable cavity length L can be made small in the order of a micron,[21] and from Eq. (8), the mode separation $\Delta\nu$ accordingly becomes large. Such a condition allows only one mode to be solely excited as shown in Fig. 3(c), excluding all the other modes outside the gain bandwidth of the laser medium. The output of such a single-mode laser becomes a continuous sinusoidal wave of a virtually infinite coherence length that is

$$l_{\mathrm{c}} = \frac{2\ln 2}{\pi}\frac{\lambda^2}{\Delta\lambda_{\mathrm{FWHM}}}, \tag{9}$$

where $\Delta\lambda_{\mathrm{FWHM}}$ is the full-width at half-maximum (FWHM) bandwidth of the single-mode spectrum.

Owing to the extended coherence length, the light signals from the reference and the sample arms would constructively interfere at countless positions of Δz_{r} so long as $2k(\Delta z_{\mathrm{s}} - \Delta z_{\mathrm{r}})$ is a multiple of 2π, thus the TD-OCT type analysis is incapable of identifying the exact point of reflection, Δz_{s}, by scanning the reference arm length Δz_{r}.

As an alternative method, the wavelength λ and thus the wavenumber $k(= 2\pi/\lambda)$ of the probe light itself can be scanned using a wavelength-tunable single-mode LD. When the wavelength is monotonically scanned from λ to $\lambda + \Delta\lambda$ as shown in Fig. 4(a), the corresponding change of the wavenumber is

$$\Delta k = \frac{2\pi}{\lambda} - \frac{2\pi}{\lambda + \Delta\lambda} \simeq 2\pi\frac{\Delta\lambda}{\lambda^2}, \tag{10}$$

where $\Delta\lambda \ll \lambda$ is presumed. Provided that this causes N cycles of cos $2k(\Delta z_{\mathrm{s}} - \Delta z_{\mathrm{r}})$ as shown in Fig. 4(b), then the location of the reflection point Δz_{s} is found by

$$4\pi\frac{\Delta\lambda}{\lambda^2}(\Delta z_{\mathrm{s}} - \Delta z_{\mathrm{r}}) = 2\pi N$$

$$\Delta z_{\mathrm{s}} = \frac{\lambda^2 N}{2\Delta\lambda} + \Delta z_{\mathrm{r}}. \tag{11}$$

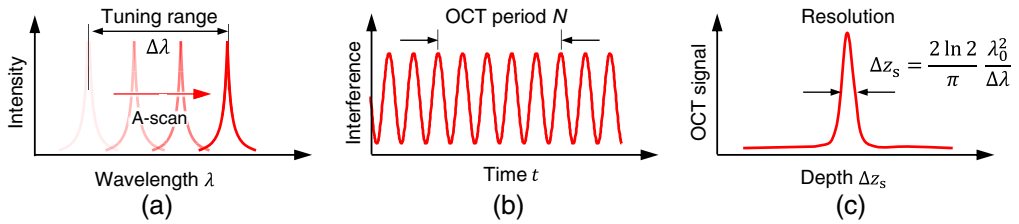

Fig. 4 Principle of swept-source OCT using a single-mode laser. (a) Wavelength tuning for A-scan and (b) oscillation signal of OCT interference when sweeping the source wavelength, which is fast Fourier transformed in (c) to find the location of the reflection point.

The number of cyclic change, N, is known by counting the interference fringes of the OCT signal or using PC-based fast Fourier transform (FFT) analysis. Due to the relation that $\Delta\lambda \ll \lambda$, the span of imaging depth can be made large and therefore suitable for ophthalmic observation.[22,23]

The axial imaging resolution is equivalent to the counting accuracy of N in Eq. (11). Provided that the difference between N and $N+1$ is resolvable by measurement, the resolution is on the order of $\lambda^2/(2\Delta\lambda)$. When the single-mode spectrum is modeled by the Gaussian profile, the longitudinal resolution is written in a more precise form as[16]

$$\Delta z_s = \frac{2\ln 2}{\pi}\frac{\lambda_0^2}{\Delta\lambda}, \tag{12}$$

where λ_0 is the center wavelength of tuning. In contrast to TD-OCT, this methodology is usually referred to as SS-OCT. Owing to the short cavity length of VCSEL and the resulting small mechanical modulation range, SS-OCT can be performed at a relatively fast frame rate. It is also capable of deep A-scan owing to the long coherence length, as a consequence of the single-mode spectrum of the emitting LD.

3 Wavelength-Tunable VCSEL Structures

Wavelength-tunable VCSELs are categorized in two types, optically pumped[24–26] and electrically pumped (current injection),[27–29] depending on how the excitation power is introduced into the active layer. Optical pumped LDs usually have a large laser gain that leads to a relatively wide wavelength tuning range and large output power. Nevertheless, cost and reliability are significant drawbacks due to the complexity of device structures that require extra optical components. In this work, we adopted an electrically pumped half-VCSEL for the simplicity of the optics involved.

Figure 5(a) schematically illustrates the assembled structure of the MEMS tunable VCSEL developed in this work. A half-cavity VCSEL chip with a gain medium of strained InGaAs multi-quantum on a standard (100) GaAs substrate is developed in-house, in a layered structure similar to the one reported elsewhere;[30] no distributed Bragg reflector (DBR) is used as an upper reflector in the VCSEL chip but it is face-side-down coupled to an electrostatically controlled MEMS diaphragm mirror made of a silicon-on-insulator (SOI) wafer to form a tunable Fabry–Perot interferometer. As a half-cavity VCSEL, the upper surface of the MEMS mirror (facing inward the laser cavity) is high reflective-coated with SiO_2/Ta_2O_5 multilayer, whereas the bottom surface is antireflective-coated with SiO_2/Ta_2O_5 multilayer for an optical outlet. The two

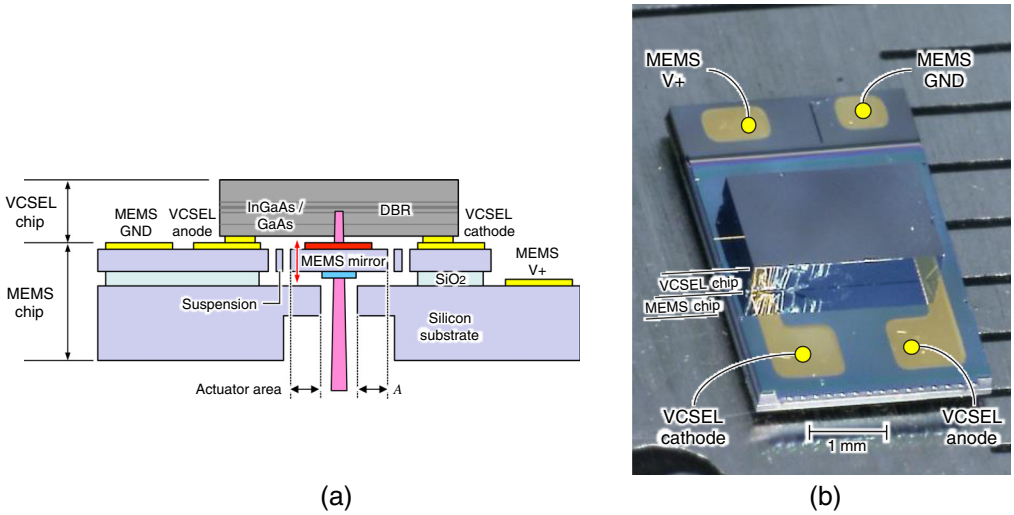

Fig. 5 Structure of the wavelength tunable LD. (a) Schematic illustration of chip assembly, an InGaAs chip on a silicon MEMS chip. (b) A VCSEL chip mounted on an electrostatic MEMS Fabry–Perot mirror.

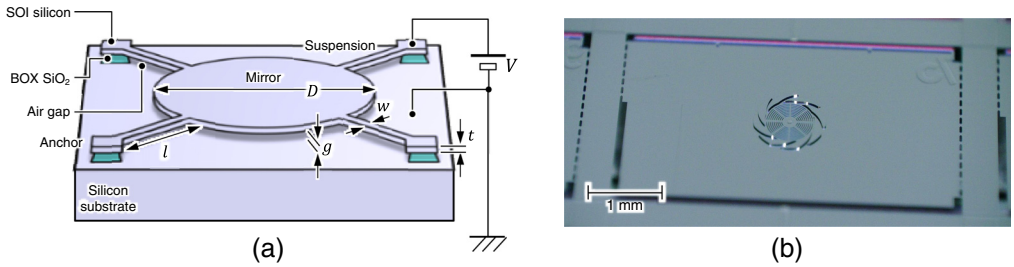

Fig. 6 MEMS mirror structure for electrostatic operation. The mirror disk is suspended above the chip with an air gap made after selective sacrificial etching of the buried oxide. (a) Schematic structure as an analytical model and (b) a photograph of a bare chip before die-bonding.

chips are assembled by thermo-compression bonding of the gold contact pads. The parallelism of the cavity is controlled by *in-situ* optical calibration of the height of the bonding pads using a dedicated measurement instrument during the bonding process. Figure 5(b) shows a finished chip photographed from the top. The chip will be later mounted on a metallic case with a hole so that the emitted light can be coupled to an optical fiber welded behind the case.

The MEMS mirror is a disk diaphragm suspended with silicon hinges as schematically illustrated in Fig. 6(a), all made in the single crystalline layer of SOI. The voltage for electrostatic operation is applied to the suspended SOI structure with respect to the handle substrate so that the cavity length in the InGaAs layer is increased due to the electrostatic pull-down of the mirror's height. Detail dimensions of the mirror and the suspensions are summarized in Table 1. The device parameters are chosen so that the fundamental mechanical resonant frequency is set around 80 kHz, and the operation voltage does not exceed 200 V_{dc} to achieve electrostatic pull-in. The actual operation voltage is lower than this upper limit, as the mirror's stroke length is augmented through mechanical resonance. Figure 6(b) shows a photograph of the MEMS mirror chip seen from the SOI side before die-bonding.

4 Optical Performance

Figure 7(a) shows the apparatus for optical performance measurement. The output of the tunable VCSEL is coupled to a multi-mode optical fiber and characterized using the optical spectrum

Table 1 Design parameters for MEMS Fabry–Perot interferometer mirror.

Item	Symbol	Dimension
Mirror disk		
Diameter	D	780 μm
Thickness	t	30 μm
Suspension bars		
Width	w	20 μm
Length	l	300 μm
Thickness	t	30 μm
Number	N	4 to 10
Electrostatic actuator		
Effective area	$A = \pi(D/2)^2 \times 80\%$[a]	3.8×10^5 μm^2
Gap length (= box thickness)	g	4 μm

[a]80%: Average fill-factor considering the distributed release holes.

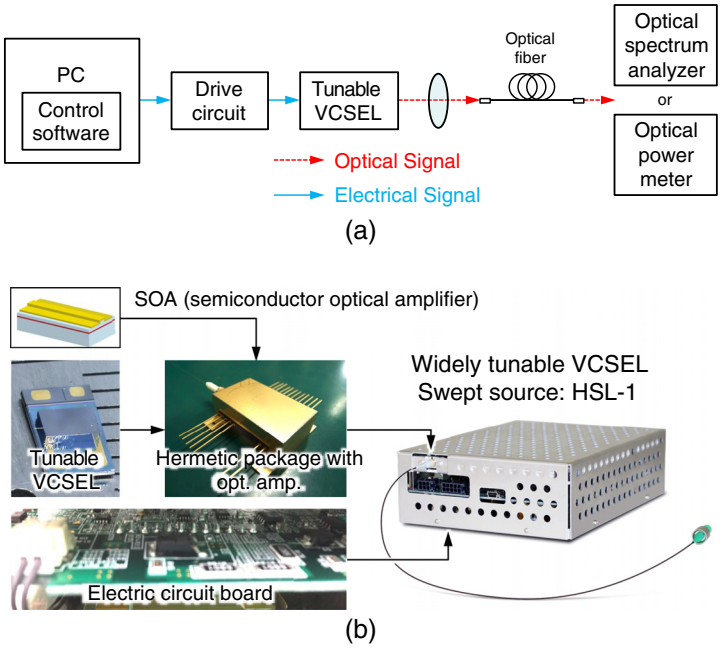

Fig. 7 Optical apparatus for characterization. (a) Block diagram for optical performance measurement and (b) VCSEL swept-source module with a MEMS tunable VCSEL and SOA.

analyzer and power meter. Figure 7(b) shows an example of a wavelength-tunable LD module assembled with a MEMS-controlled VCSEL chip. Semiconductor components such as VCSEL, SOA, and optical components were hermetically assembled in a sealed package, and controlled by an electrical circuit interface that provides both the injection current for the tunable VCSEL module and the electrostatic control voltage for the MEMS. The LD unit also gives a start trigger (A-trigger) for the depth scan (A-scan) that could be used to initiate the spatial beam steering (B-scan), for which MEMS optical scanners are frequently used.[31–34] It also generates another sampling trigger (K-trigger) at an equal wavelength interval.

Figure 8 shows the optical output power as a function of injection current, measured at the peak power wavelength (1065 nm). The threshold current was 0.44 mA, and maximum deliverable power was 1.5 mW at an injection current of 8 mA. OCT measurement usually requires a probe power of more than 10 mW, and we therefore used a semiconductor optical amplifier (SOA) in the subsequent stage to enhance the output power of the LD module to 30 mW.

Figure 9 shows the lasing spectrum of the developed tunable LD, measured using an optical spectrum analyzer (AQ6370D, Yokogawa Test & Measurement Corporation) near the peak power wavelength. A single-mode resonance was realized by appropriately designing the resonator's FSR to be wider than the effective band of the DBR. The side-mode suppression ratio

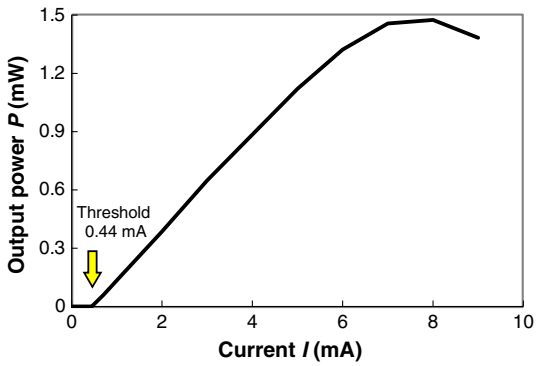

Fig. 8 Output power of LD as a function of injection current.

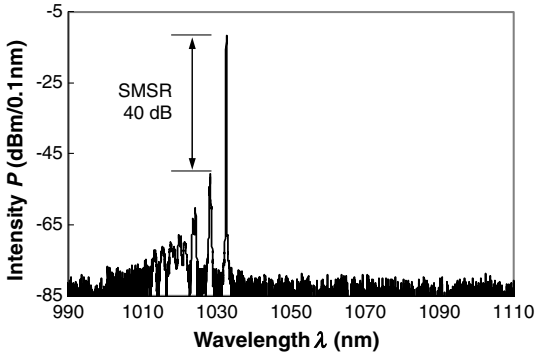

Fig. 9 Intensity spectrum of LD. SMSR of at least 40 dB is confirmed.

(SMSR) was tuned to be greater than 40 dB by optimizing the aperture dimensions of the VCSEL and the MEMS mirror disk. This SMSR is sufficient to make the LD acceptable as a single-mode light source.

Output power profiles of the VCSEL (injection current 6 mA) were determined as shown in Fig. 10(a), at different dc voltages applied to control the cavity length of the electrostatic MEMS mirror. Individual longitudinal modes of above 25 dB were obtained over the whole tuning range between 1010 and 1090 nm when the MEMS mirror was operated with dc voltages of 100 to 190 V, as shown in Fig. 10(b). Continuous wavelength control over 89 nm with respect to the center wavelength 1050 nm was confirmed at room temperature without causing mode hopping. No laser output was observed for dc voltages of lower than 100 V because the wavelengths corresponding to the cavity lengths were outside the gain bandwidth of the laser medium. When the MEMS mirror was electrostatically operated at 100 kHz, the operation voltage could be lowered to 124 V_{ac} to achieve a continuous wavelength sweep in the same range as shown in Fig. 11; the spectrum was obtained by keeping the gate of spectrum analyzer open for 10 s to accommodate more than 10^6 cycles of the wavelength scan. In addition, oscillation of the mirror at the resonant frequency (80 kHz) was found to be susceptibly influenced by the environment change. Therefore, we used a frequency slightly higher than the resonance (100 kHz) to set a margin in the oscillation amplitude so that the control electronics could maintain the oscillation level by adjusting the drive voltage.

Figure 12 shows the temporal changes in the optical output power and the lasing wavelength scanned at 50 kHz. Unlike piezoelectrically driven actuator whose displacement is proportional to the applied voltage, the electromechanical behavior of the mirror in this work is described using an electrostatic parallel plate model whose displacement changes as a quadratic function of applied voltage when actuated at a frequency well below the mechanical resonance. As a result, the lasing wavelength also follows a quadratic function of the voltage, which is not convenient

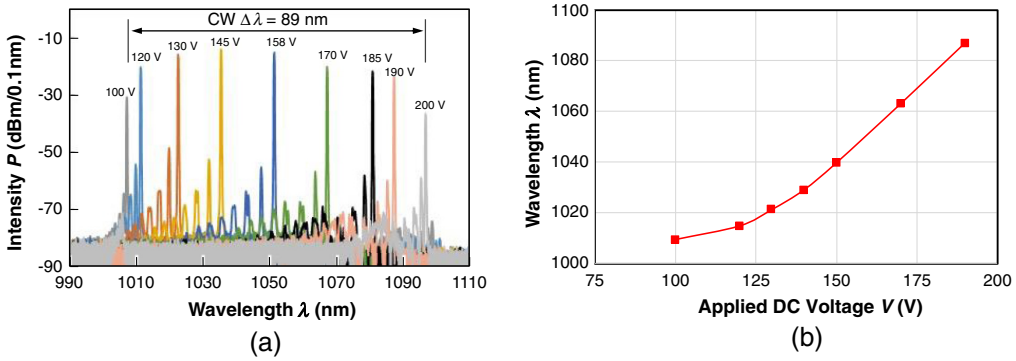

Fig. 10 Wavelength tuning performance measured at different dc voltages applied to control the cavity length of the electrostatic MEMS mirror. (a) Spectrum range of tuning more than 89 nm. (b) Center wavelength as a function of operation voltage of the MEMS Fabry–Perot mirror.

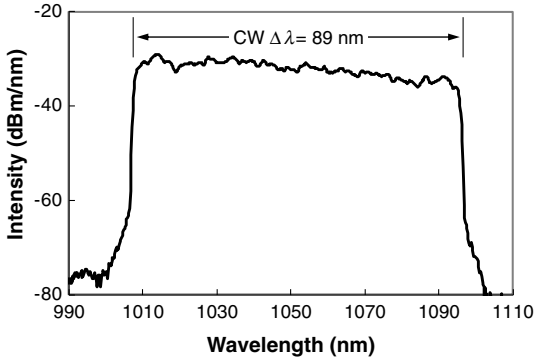

Fig. 11 Continuous wavelength tuning with a MEMS mirror operated by a sinusoidal wave voltage at 100 kHz.

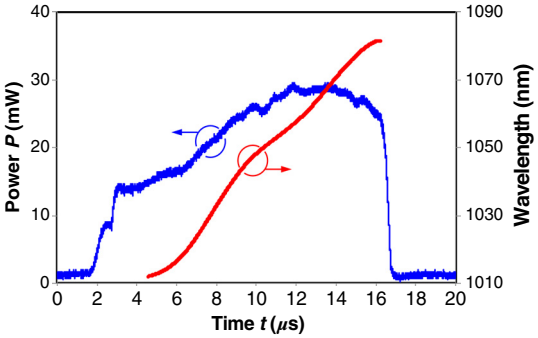

Fig. 12 Wavelength sweep performance (power and wavelength) when operated at 50 kHz.

when performing FFT analysis that presumes a uniform frequency step size. Therefore, we used the K-trigger from the LD module to rearrange the acquired data into data strings of a uniform wavelength step. This data processing allowed the SS-OCT to function in a wide range of operation frequencies between 4 and 200 kHz. The swept-source operation can be performed at a frequency higher than the mechanical resonance (80 kHz) of the MEMS because wavelength tuning takes place during both strokes. Typical optical output power above 30 mW was obtained with the use of an SOA and when modulated at a duty ratio of 50%, more than 15 mW of optical power could be delivered to the OCT system, which meets the signal power requirements of most OCT applications for medical diagnosis.

Owing to the single-mode resonance, the developed tunable VCSEL was expected to have a long coherence length of more than 100 m. We used a fiber-coupler Michelson–Morley interferometer, as schematically shown in Fig. 13(a), to determine the roll-off of the fringe

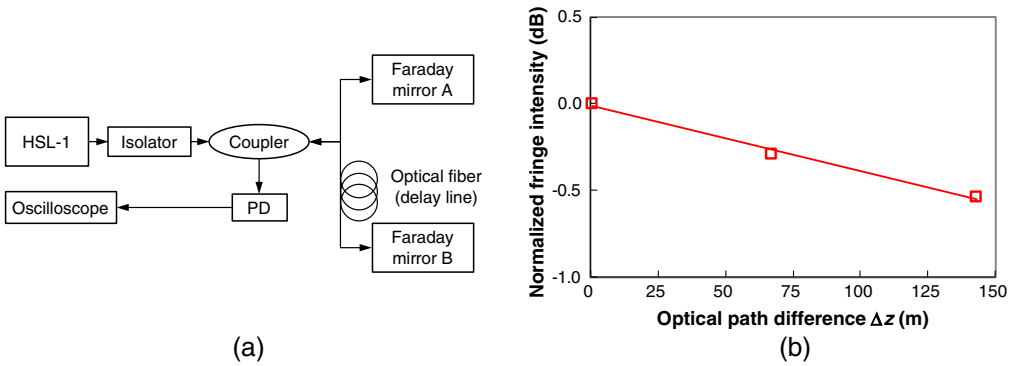

Fig. 13 Coherence length measurement of the developed light source. (a) Block diagraph of measurement apparatus and (b) measurement result showing a coherence length of more than 150 m.

interference intensity as a function of the path difference Δz, as shown in Fig. 13(b); the travel distance has been converted to that in air taking the refractive index of the optical fiber into account, and the fringe intensity has been normalized by the value taken for $\Delta z = 0$. The coherence length, defined as the length beyond which the interference intensity attenuates by more than -3 dB, is thus shown to be longer than 150 m because the experimentally determined loss was no greater than -0.5 dB at this length of optical path difference. The result suggested that the developed light source could also be used for long range LiDAR application.[15]

5 SS-OCT Performance

Figure 14 shows the block diagram of the SS-OCT system using a wavelength tunable VCSEL. The probe light from the light source is spatially scanned over the sample with a Galvano scanner, and its interference signal is received by a balanced photodetector (BPD). Analog-to-digital conversion is performed at 500 MHz using a data acquisition module (Flexible SS-OCT DAQ Board HAD-5200B-S, Santec Corporation) and an FFT on a personal computer (PC) to calculate the depth of the light-reflective feature in the sample. The PC also controls the Galvano scanner by the analog voltages applied through an amplifier (Amp).

Owing to the wide tunable wavelength range and the fast modulation speed, SS-OCT was performed through different ranges of measurement depth using a single light source. Figure 15(a) shows an OCT image of a human eye, when the wavelength tuning range was set to be 40 nm. The scan speed of the wavelength was 20 kHz, and the data were acquired at 50% duty ratio, when the wavelength was swept upward only. Due to the fast frame rate of 40 fps, a clear OCT image was obtained without being affected by motion due to fibrillation in the eye muscles. The single-mode nature of the VCSEL also allowed a relatively large FSR, and thus a long coherence revival length, which allows us to image the entire eye in a single shot, including the anterior chamber and the retina. The axial length of the eye was instantly measured to be 25 mm, which was in the normal range for adults.

In addition to SS-OCT measurements over a short working distance such as ophthalmologic observation, the same optical system could also be used over longer distances when the wavelength tuning range was deliberately reduced by reprogrammable software. Figure 16(a) shows an object made of opaque plastic bricks placed at a 50-cm distance from the OCT aperture. By measuring the surface reflection, a 3D profile image of the object was reconstructed as shown in Fig. 16(b). Due to the long coherence length of over 150 m, OCT measurement of a relatively large object was thus possible without suffering from the coherence revival problem; this result implies that the SS-OCT system developed in this work could be used for alternative applications such as surface profilometry or laser range finding.

Figure 17 compares the quality of SS-OCT images obtained using a conventional multi-mode LD and a single-mode VCSEL. A reel of semi-transparent adhesive tape placed in front of the OCT aperture was observed at four different distances. At the initial position, $\Delta z = 0$, images of both the multi-mode LD and the single-mode VCSEL clearly presented the layered structure of adhesive tape as shown in Figs. 17(a1) and 17(b1), respectively. When the reel was retracted by 3 mm, the images were equally displaced downward as shown in Figs. 17(a2) and 17(b2) until

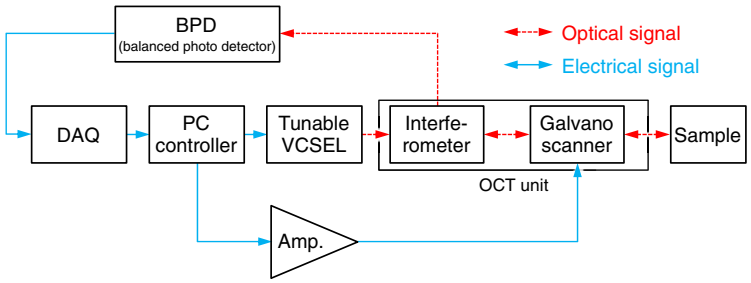

Fig. 14 Optoelectrical block diagram for SS-OCT.

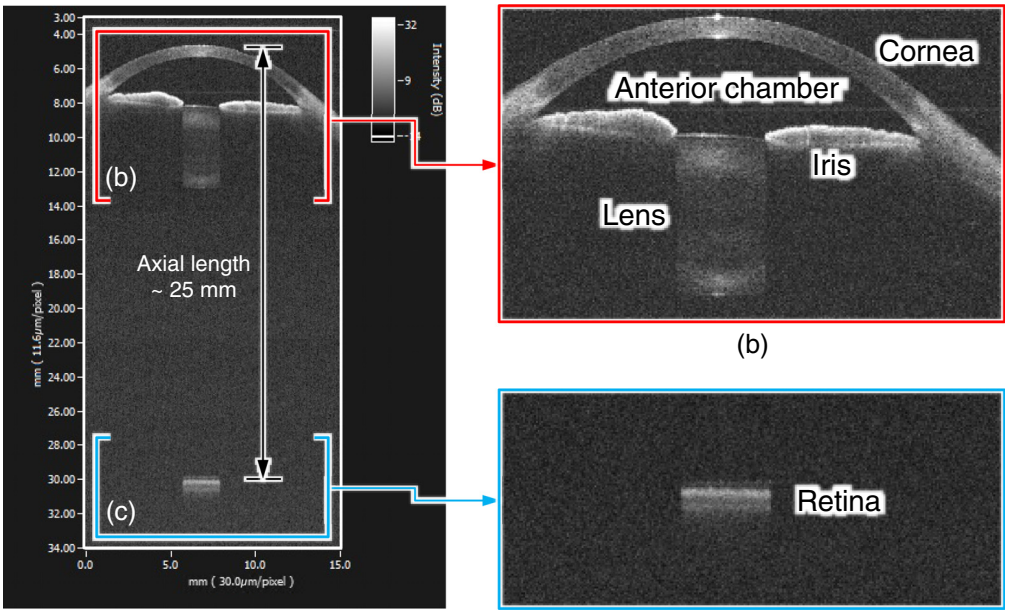

Fig. 15 OCT image of human ocular globe. (a) Entire view obtained by a single shot OCT, (b) close up image of the anterior chamber and the lens, and (c) close up image of the retina.

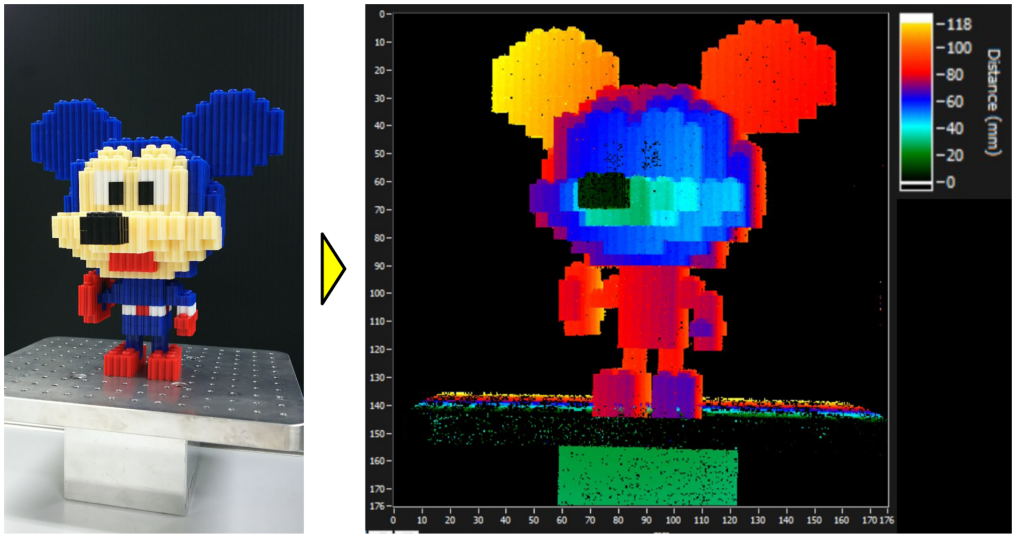

Fig. 16 Three-dimensional profile measurement by OCT over a long distance. (a) Target object placed at a 50-cm distance from the OCT system and (b) its color map profile.

they slid off the field of view as shown in Figs. 17(a3) and 17(b3). When the object is retracted further, the OCT image should remain as blank as Fig. 17(b4) obtained by the single-mode VCSEL. However, the image obtained by the multi-mode LD presented a ghost image as shown in Fig. 17(a4). This artifact was caused by the repetition of wave packets shown in Fig. 3(b), which produced the false intensity-modulated signal affecting the FFT computation to determine the depth of reflection.

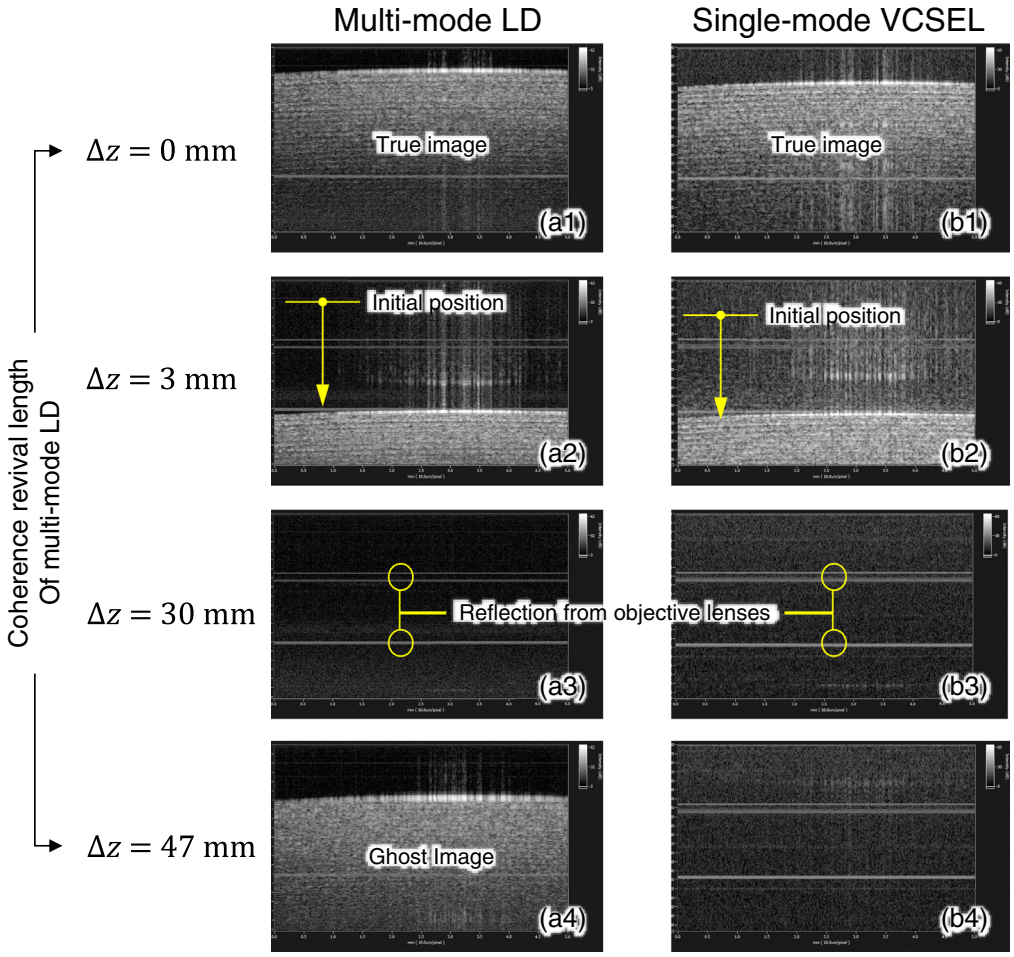

Fig. 17 Comparison of OCT images obtained with (a1)–(a4) a multi-mode LD and (b1)–(b4) a single-mode LD.

6 Conclusions

Wavelength tunable VCSELs are one of the most appropriate applications of optical microsystems based on MEMS technology. A short-cavity LD can be assembled by putting a VCSEL chip onto an electrostatically tunable MEMS Fabry–Perot interferometer to realize a single-mode wavelength-tunable LD of a long coherence length as well as a long coherence revival length. In this work, an electrostatically actuated MEMS diaphragm mirror of 780 μm in diameter was developed by silicon micromachining using an SOI substrate and coupled with an InGaAs VCSEL chip to produce a wavelength-tunable VCSEL with a wide tuning range of 89 nm around a center wavelength of 1050 nm. Typical output power of 1.5 mW was obtained from an injection current of 8 mA. As a result of the short cavity length, the coherence length was longer than 150 m, which made the device suitable as a light source for an SS-OCT system that could be used to measure the ophthalmic axial length at high speed under 25 ms. In addition to ocular characterization, the same system was also found to be capable of performing long-range measurements, such as surface profilometry, LiDAR, and laser welding monitoring.

Acknowledgments

The authors thank the R&D team members of Santec Corporation for their experimental help and technical discussions. The authors have no relevant financial interests in the paper and no other potential conflicts of interest to disclose.

References

1. N. M. Bressler, "Reducing the progression of myopia," *J. Am. Med. Assoc.* **324**(6), 558–559 (2020).
2. V. Navel, S. Beze, and F. Dutheil, "COVID-19, sweat, tears… and myopia?" *Clin. Exp. Optometry* **103**(4), 555–555 (2020).
3. F. F. Li et al., "Differential effects on ocular biometrics by 0.05%, 0.025%, and 0.01% atropine," *Ophthalmology* **127**(12), 1603–1611 (2020).
4. O. Hieda et al. "Efficacy and safety of 0.01% atropine for prevention of childhood myopia in a 2-year randomized placebo-controlled study," *Jpn. J. Ophthalmol.* **65**, 315–325 (2021).
5. G. Marchini et al., "Ultrasound biomicroscopic and conventional ultrasonographic study of ocular dimensions in primary angle-closure glaucoma," *Ophthalmology* **105**(11), 2091–2098 (1998).
6. I. Matsumura et al., "The design of an open view autorefractometer," in *Proc. 2nd Int. Symp. Adv. Diagn. Vis. Opt.*, Tucson, Arizona, pp. 36–42 (1982).
7. K. Takada et al., "New measurement system for fault location in optical waveguide devices based on an interferometric technique," *Appl. Opt.* **26**(9), 1603–1606 (1987).
8. D. Huang et al., "Optical coherence tomography," *Science* **254**(5035), 1178–1181 (1991).
9. K. Iga, "Forty years of vertical-cavity surface-emitting laser: invention and innovation," *Jpn. J. Appl. Phys.* **57**, 08PA01 (2018).
10. K. Isamoto et al., "Electrically pumped MEMS-based tunable VCSEL of wide wavelength range for SS-OCT," in *Proc. Int. Conf. Opt. MEMS and Nanophotonics (IEEE OMN 2019), KAIST*, Daejeon, pp. 90–91 (2019).
11. T. Yonetsu et al., "Optical coherence tomography—15 years in cardiology," *Circul. J.* **77**(8), 1933–1940 (2013).
12. A. Baumgartner et al., "Polarization-sensitive optical coherence tomography of dental structures," *Caries Res.* **34**, 59–69 (2000).
13. J. Welzel, "Optical coherence tomography in dermatology: a review," *Skin Res. Technol.* **7**, 1–9 (2001).
14. K. Kim et al., "Non-destructive identification of weld-boundary and porosity formation during laser transmission welding by using optical coherence tomography," *IEEE Access* **6**, 76768–76775 (2018).
15. M. Okano and C. Chong, "Swept source lidar: simultaneous FMCW ranging and nonmechanical beam steering with a wideband swept source," *Opt. Express* **28**(16), 23898–23915 (2020).
16. J. A. Izatt and M. A. Choma, "Theory of optical coherence tomography," in *Optical Coherence Tomography: Technology and Applications*, W. Drexler and J. G. Fujimoto, Eds., Springer, Berlin Heidelberg (2008).
17. A.H. Dhalla, D. Nankivil, and J. A. Izatt, "Complex conjugate resolved heterodyne swept source optical coherence tomography using coherence revival," *Biomed. Opt. Express* **3**(3), 633–649 (2012).
18. Y. Watanabe et al. "Axial-lateral parallel time domain OCT with an optical zoom lens and high order diffracted lights for variable imaging range," *Opt. Express* **15**(8), 5208–5217 (2007).
19. A. Q. Liu and X. M. Zhang, "A review of MEMS external-cavity tunable lasers," *J. Micromech. Microeng.* **17**, R1–R13 (2007).
20. K. Totsuka et al., "MEMS scanner based swept-source laser for optical coherence tomography," *Proc. SPIE* **7554**, 75542Q (2010).
21. C. J. Chang-Hasnain, "Tunable VCSEL," *IEEE J. Sel. Top. Quantum Electron.* **6**, 978–987 (2000).
22. A. F. Fercher et al., "Measurement of intraocular distances by backscattering spectral interferometry," *Opt. Commun.* **117**, 43–48 (1995).
23. R. Leitgeb, C. K. Hitzenberger, and A. F. Fercher, "Performance of Fourier domain vs. time domain optical coherence tomography," *Opt. Express* **11**(8), 889–894 (2003).
24. H. K. Sahoo et al., "Tunable MEMS VCSEL on silicon substrate," *IEEE J. Sel. Top. Quantum Electron.* **25**(6), 1700707 (2019).

25. V. Jayaraman et al., "Recent advances in MEMS-VCSELs for high performance structural and functional SS-OCT imaging," *Proc. SPIE* **8934**, 893402 (2014).
26. D. D. John et al., "Wideband electrically pumped 1050-nm MEMS-tunable VCSEL for ophthalmic imaging," *J. Lightwave Technol.* **33**(16), 3461–3468 (2015).
27. G. D. Cole et al., "Short-wavelength MEMS-tunable VCSELs," *Opt. Express* **16**(20), 16093–16103 (2008).
28. T. Yano et al., "Wavelength modulation over 500 kHz of micromechanically tunable InP-based VCSELs with Si-MEMS technology," *IEEE J. Sel. Top. Quantum Electron.* **15** (3), 528–534 (2009).
29. M. Kuznetsov et al., "Compact ultrafast reflective Fabry–Perot tunable lasers for OCT imaging applications," *Proc. SPIE* **7554**, 75541F (2010).
30. N. Nishiyama et al., "Multi-oxide layer structure for single-mode operation in vertical-cavity surface-emitting lasers," *IEEE Photonics Technol. Lett.* **12**(6), 606–608 (2000)
31. C. Gorecki and S. Bargiel, "MEMS scanning mirrors for optical coherence tomography," *Photonics* **8**, 6 (2021).
32. M. Nakada et al., "Optical coherence tomography by all-optical MEMS fiber endoscope," *IEICE Electron. Express* **7**(6), 428–433 (2010).
33. J. Sun et al., "3D *In vivo* optical coherence tomography based on a low-voltage, large-scan-range 2D MEMS mirror," *Opt. Express* **18**(12), 12065–12075.
34. H.-C. Park et al., "Forward imaging OCT endoscopic catheter based on MEMS lens scanning," *Opt. Lett.* **37**(13), 2673–2675 (2012).

Mohammed S. Khan is a lead expert at Santec Corporation. He received his BS and MS degrees in electronic engineering from the University of Osaka in 1995 and 1997, respectively. His current research interests include semiconductor devices and optoelectronic systems. He is a member of the Optical Society (OSA).

Changdae Keum is a specialist at Santec Corporation. He received his BS and MS degrees in polymer chemistry from Kyungpook National University, Korea, in 1996 and 1998, respectively, and his PhD in environmental chemistry and engineering from Tokyo Institute of Technology, Japan, in 2001.

Yi Xiao received his BS and MS degrees in electronic engineering from Zhejiang University, China, in 2009 and 2012, respectively, and his PhD in electrical engineering from the University of Tokyo, Japan, in 2018. His current research interests include semiconductor laser and MEMS.

Keiji Isamoto received his BS and MS degrees in electrical and engineering from Toyohashi University of Technology, Aichi, Japan, in 1994 and 1996, respectively. He joined Central R&D Laboratory of OMRON Co. in 1996 and was engaged in the development of micro-optics. He joined Santec Corporation, Japan, in 2001, and worked on several subjects including optical hybrid module, MEMS-based variable optical attenuator and high-speed swept laser for OCT. He received his PhD in electrical engineering from the University of Tokyo, Tokyo, Japan, in 2016. Since 2018, he has been a president of Optical Imaging and Sensing Company in Santec Corporation. His research interests include optical MEMS and OCT for medical and industrial application.

Nobuhiko Nishiyama received his BE, ME, and PhD degrees from Tokyo Institute of Technology, Japan, in 1997, 1999, and 2001, respectively. During his PhD work, he demonstrated single-mode 0.98- and 1.1-μm-VCSEL arrays with stable polarization using misoriented substrates for high-speed optical networks and MOCVD-grown GaInNAs VCSELs. He joined Corning, Inc., New York, in 2001, and worked with the Semiconductor Technology Research Group. At Corning, he worked on several subjects including short-wavelength lasers, 1060-nm DFB/DBR lasers, and long-wavelength InP-based VCSELs. In 2006, he became an associate professor with the Tokyo Institute of Technology. After that, he worked for 1.3-μm transistor lasers, terahertz–optical signal conversion devices. Since 2020, he has been a professor. His current interests are silicon photonics, III–V/SOI hybrid PICs, membrane PICs, and LiDAR. He was the recipient of the Excellent Paper Award from the Institute of Electronics,

Information, and Communication Engineers (IEICE) of Japan in 2001; the Young Scientists' Prize of the Commendation for Science and Technology from the Minister of Education, Culture, Sports, Science, and Technology in 2009; and the Ichimura Prize in Science for Distinguished Achievement in 2016.

Hiroshi Toshiyoshi received his BS, ME, and PhD degrees in electrical engineering from the University of Tokyo, Tokyo, Japan, in 1991, 1993 and 1996, respectively. He joined the Institute of Industrial Science, the University of Tokyo in 1996 as a lecturer. From 1999 to 2001, he was a visiting assistant professor at the University of California, Los Angeles, USA. In 2002, he became an associate professor with the Institute of Industrial Science (IIS), the University of Tokyo. From 2002 to 2007, he was a codirector of LIMMS/CNRS-IIS UMI-2820, an international joint laboratory of the Centre National de la Recherche Scientifique, Paris, France. Since 2009, he has been a professor with the IIS, the University of Tokyo. His research interests include optical MEMS, power MEMS, and CMOS-MEMS.